Research paper

Struct Multidisc Optim 26, 50–66 (2004)
DOI 10.1007/s00158-003-0301-z

Topology optimization of continuum structures with material failure constraints

J.T. Pereira, E.A. Fancello and C.S. Barcellos

Abstract This work presents an efficient strategy for dealing with topology optimization associated with the problem of mass minimization under material failure constraints. Although this problem characterizes one of the oldest mechanical requirements in structural design, only a few works dealing with this subject are found in the literature. Several reasons explain this situation, among them the numerical difficulties introduced by the usually large number of stress constraints. The original formulation of the topological problem (existence/non-existence of material) is partially relaxed by following the SIMP (Solid Isotropic Microstructure with Penalization) approach and using a continuous density field ρ as the design variable. The finite element approximation is used to solve the equilibrium problem, as well as to control ρ through nodal parameters. The formulation accepts any failure criterion written in terms of stress and/or strain invariants. The whole minimization problem is solved by combining an augmented Lagrangian technique for the stress constraints and a trust-region box-type algorithm for dealing with side constraints ($0 < \rho_{\min} \leq \rho \leq 1$). Numerical results show the efficiency of the proposed approach in terms of computational costs as well as satisfaction of material failure constraints. It is also possible to see that the final designs define quite different shapes from the ones obtained in classical compliance problems.

Received: 14 March 2002
Revised manuscript received: 26 January 2003
Published online: 10 September 2003

J.T. Pereira[1], E.A. Fancello[2,✉] and C.S. Barcellos[3]

[1] Departamento de Engenharia Mecânica, Centro Federal de Educação Tecnológica do Paraná (CEFET/PR), Curitiba, PR, 80230-901, Brazil
e-mail: jucelio@cefetpr.br
[2] Departamento de Engenharia Mecânica, Universidade Federal de Santa Catarina, Florianópolis, SC, 88010-970, Brazil
e-mail: fancello@grante.ufsc.br
[3] IPUC, Pontifícia Universidade Católica de Minas Gerais, Belo Horizonte, MG, CEP 30535-610, Brazil
e-mail: clovis@pucminas.br

1 Introduction

Design is a key aspect of any marketing concept in which products must change and improve their capabilities to fit customer needs. This paradigm has led to the shortening of design and production cycles in order to maintain competitiveness in a very aggressive business environment.

On the other hand, from a more holistic point of view, social constraints have recently oriented the production of material goods in accordance with ecological precepts, which has also stimulated the re-design and optimization of current products.

As a consequence of this scenario, optimization has received increasing attention and has taken an important place in the activities of designers. This fact can be easily appreciated if one considers the great number of commercial analysis software packages equipped with optimization modules.

Topological optimization is probably one of the newest features incorporated in these tools. Its ability to suggest initial drawings and conceptual designs has attracted the attention of designers, and it is presently a fertile area of research.

The specific problem of minimizing flexibility for a given amount of material, widely known as the Compliance Problem, occupies more than 90% of the research work in topology optimization of mechanical devices. The reasons for this focus stem from the mathematical properties of the problem to the historical trends of its development. However, despite its well-developed mathematical background and its numerical properties, this problem is not necessarily representative of the most frequent requirements for practical applications. One of the most intuitive questions in mechanical design is still the following: what is the lightest design that operates without material failure? This objective can be written in short as

$$\begin{aligned} &\text{Minimize} \quad \text{Mass} \\ &\text{Subject to}: \; F\left(\sigma\left(\mathbf{x}\right)\right) \leq 0\,, \quad \forall\ \mathbf{x} \in \Omega\,. \end{aligned} \tag{1}$$

The material failure function F depends on the stress field $\sigma\left(\mathbf{x}\right)$ and strain field $\varepsilon\left(\mathbf{x}\right)$, and all of them are defined in an original domain Ω.

A large set of questions then arises: What does a material constraint physically mean in a topological problem? How should it be written? Should this constraint be local in a strict sense (pointwise)? It is more or less obvious that, if not pointwise, some kind of local evaluation of failure should be performed, which will generate an appreciable number of discrete constraints in the equivalent numerical problem. This is one of several important differences between this and the compliance problems and probably constitutes one of the reasons for the small number of works dealing with this kind of problem in the literature.

2
A brief review

A problem that is similar to the present one is called the Fully Stressed Design (FSD) approach. Its main assumption is the existence of a design for which all material points have their stress-based failure constraint saturated. In this case, an optimality condition may be written. Initially applied to frame structures this approach was also extended to 2D problems (Cursi and Pagnaco 1995; Novotny *et al.* 1998).

Evolutionary Structural Optimization (ESO) is also a FSD-like approach, whose principles may be found in the works of Querin *et al.* (1998). It is based on the idea of removing material from low-stressed regions and adding material in the opposite case, and it is for this reason that the algorithm is called *bidirectional*. The same authors call a variation of this idea an *additive* algorithm (Querin *et al.* 2000). An initial design, formed by a small number of elements "grows" by an element addition process guided by the minimization of a performance function (Performance Index) given by

$$PI = \frac{1}{PL}\int \sigma_{vM}\,\mathrm{d}\Omega\,,$$

where σ_{vM} is the von Mises effective stress field, P is a representative force of the external load and L a characteristic dimension of the model.

Returning to statement (1), some authors use as the failure material constraint a *p-norm* of the von Mises stress field:

$$\left\|\frac{\sigma_{vM}}{\sigma_{adm}}\right\|_{L^p(\Omega)} = \left[\int\left(\frac{\sigma_{vM}}{\sigma_{adm}}\right)^p \mathrm{d}\Omega\right]^{1/p}, \qquad (2)$$

where σ_{adm} is the admissible von Mises stress. Yang and Chuang (1994), Park (1995) and Yang and Chen (1996) considered as the objective function a linear combination of the internal strain energy and the above functional. All of them are based on microstructure designs of the SIMP (Solid Isotropic Microstructure with Penalization) type (Bendsøe 1995).

Shim and Manoochehri (1997) treated the problem (2) through Simulated Annealing based also on the elimination/readmission of elements in a FE mesh, as well as using discrete optimization techniques (Shim and Manoocheri 1998).

A classical nonlinear programming approach can be found in the work of Duysinx and Bendsøe (1998) and Duysinx and Sigmund (1998), in which the SIMP approach and a stress failure constraint was chosen to solve problem (1). The large-scale optimization problem was solved through the convex approximation and dual algorithms. In Duysinx (1998) the same approach was used to point out the different optimal designs obtained for materials with different failure criteria on traction and compression.

From a quite different approach, Stolpe and Svanberg (2001) used integer programming of the form 0-1 to solve problem (1). The original problem was rewritten as an equivalent linear sub-problem that was solved with branch-and-bound and branch and cut methods.

The present work formulates problem (1) following the same approach as that proposed by Duysinx and Bendsøe (1998). The formalism is just re-arranged in order to allow a general expression for material failure constraints (and derivatives) written in terms of the principal invariants of the Cauchy stress σ. Within this formulation the existence of singular optima is eliminated by using the ϵ-regularization proposed by Cheng and Guo (1997).

The numerical treatment is, however, different from the former work. The augmented Lagrangian technique is used to deal with local stress constraints, while the limits on the design variable, the density ρ, are solved with a trust-region box-type algorithm. This approach is in accordance with that adopted for the stress constraints at the formulation level, in which the regularization parameter ϵ weakens this constraint. Each local stress constraint is, in the present work, included as a penalization term in the cost function, "weighted" by a Lagrangian multiplier. Moreover, this approach produces a huge reduction of computational costs when derivatives of the problem are needed. For a given design, the gradient of the objective function is obtained using adjoint sensitivity analysis at just the cost of a back-substitution procedure and some integration effort. This choice allows the use of a large number of local stress constraints and, therefore, refined meshes.

The checkerboard phenomenon is controlled by a simple penalization term on the density gradient. This technique was proposed by Pereira (2001) following the ideas of gradient constraints from Petersson and Sigmund (1998) and Borrvall and Petersson (2001). Work was also published simultaneously by Borrvall (2001), in which the former penalization is found, and a complete theoretical and numerical discussion about this issue is given.

In order to maintain a unified notation and make the paper easily comprehensible, Sect. 3 is used to state biefly the basic formulation of the problem.

Section 4 equates this expression to the augmented Lagrangian approach. Section 5 shows the analytical sensitivity analysis of the final Lagrangian functional, while Sect. 6 presents operational details and choices of the finite element approximation of displacements, stresses and density fields. The nonlinear optimization algorithm is described in Sect. 7. Finally, Sects. 8 and 9 present a set of numerical results in which the efficiency, advantages and difficulties of the proposed approach are discussed.

3
Formulation of the problem

Let Ω be an open domain with boundary $\partial\Omega$ belonging to the physical space $\Re^n$ $(n = 1, 2, 3)$. A material body occupies the domain Ω_m, included in Ω. The complement of Ω_m in Ω is denoted by Ω_v and represents void spaces (Fig. 1). It is also assumed that the boundary of Ω_m is smooth enough and contains the part $\partial\Omega_N$ of $\partial\Omega$ where a traction $\mathbf{t}$ is applied ($\mathbf{t} \in H^{-1/2}(\partial\Omega; \Re^n)$). Classical linear elasticity is assumed to be a good representation of the body behavior. Thus, a set of constitutive, kinematic and equilibrium equations relate the constitutive elasticity tensor $\mathbf{D}$, the stress tensor $\sigma \in L^2(\Omega_m; \Re^{n\times n})$, the deformation tensor $\varepsilon \in L^2(\Omega_m; \Re^{n\times n})$ and the displacement vector $\mathbf{u} \in H^1(\Omega_m; \Re^n)$ as follows:

$$\begin{aligned} &\sigma = \mathbf{D}\varepsilon\,, \\ &\varepsilon = \nabla^S \mathbf{u} = \frac{1}{2}\left(\nabla\mathbf{u} + \nabla^T\mathbf{u}\right)\,, \\ &div\,(\sigma) = 0 \qquad \forall\,\mathbf{x} \in \Omega_m\,. \end{aligned} \tag{3}$$

The following boundary conditions also apply:

$$\begin{aligned} &\sigma\,\mathbf{n} = \bar{\mathbf{t}} \qquad \forall\,\mathbf{x} \in \partial\Omega_N \subset (\partial\Omega_m \cap \partial\Omega)\,, \\ &\sigma\,\mathbf{n} = \mathbf{0} \qquad \forall\,\mathbf{x} \in \partial\Omega_F := \partial\Omega_m \backslash (\partial\Omega_N \cup \partial\Omega_D)\,, \\ &\mathbf{u} = \bar{\mathbf{u}} \qquad \forall\,\mathbf{x} \in \partial\Omega_D \subset (\partial\Omega_m \cap \partial\Omega)\,. \end{aligned} \tag{4}$$

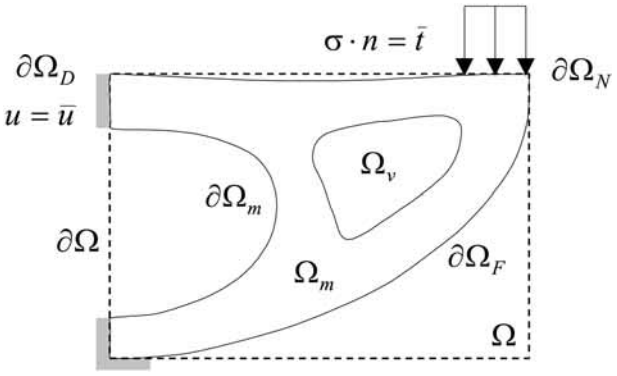

Fig. 1 Geometric definitions of a domain composed of solid and voids

The weighted-residual method applied to (3)–(4) leads to the classical variational expression in which the equilibrium displacements $\mathbf{u} \in U$ satisfy the equation:

$$B(\mathbf{u}, \mathbf{v}) = l(\mathbf{v}) \qquad \forall\,\mathbf{v} \in V\,, \tag{5}$$

where $B(\cdot,\cdot) : U \times V \to \Re$ is a symmetric bilinear form, $l : V \to \Re$ is a linear functional associated with the external loads, U and V are the kinematic admissible fields of the displacements and variations, respectively.

It is well known in the literature that formulating (1) as a problem of existence or non-existence of material (i.e., using characteristic functions) leads to an ill-posed problem and a minimum may not exist. A possible way of circumventing this inconvenience is including intermediate values between solid ($\rho = 1$) and voids ($\rho = 0$) by using "porous materials" (Bendsøe and Kikuchi 1988). Among several possible choices, this work uses the SIMP (Solid Isotropic Microstructure with Penalty) approach (Bendsøe and Sigmund 1999). Taking the relative density $0 \le \rho \le 1$ as the design variable, the constitutive behavior of the microstructure is described by relating the elasticity tensor D_ρ with the elasticity tensor of the solid material D^0 as follows:

$$\mathbf{D}_\rho = f_D(\rho)\,\mathbf{D}^0 = \rho^p \mathbf{D}^0\,. \tag{6}$$

With these assumptions in hand, the original problem may be written as a new one stated as

Problem P_1:

$$\underset{\rho \in L^\infty(\Omega;(0,1))}{\text{Min}}\; m(\rho) = \rho_0 \int_\Omega \rho(\mathbf{x})\,\mathrm{d}\Omega\,, \tag{7}$$

$$\text{Subject to}: \rho(\mathbf{x})\,F(\sigma(\mathbf{x})) \le 0 \quad \text{a.e. in } \Omega\,.$$

3.1
Material failure criterion

A material failure criterion will denote, in this context, a function capable of identifying how far a material point submitted to a quasi-static stress state is from failure. Failure may signify yielding for a ductile material or crack initiation in a fragile one. It can be stated as

$$F(\sigma_{ij},\, k_1,\, k_2,\, \ldots) = 0\,, \tag{8}$$

where the parameters $k_1,\, k_2, \ldots,$ are experimentally obtained for each material. It is assumed that failure does not occur if $F(\sigma) \le 0$.

Due to its applicability to a wide class of metallic materials and to its simplicity, the von Mises failure criterion is one of the mostly used frequent expressions, and is given by

$$F_{vM}(\sigma) = \frac{\sigma_{vM}}{\sigma_{adm}} - 1\,, \tag{9}$$

where σ_{adm} is the material yielding stress and σ_{vM} is the effective von Mises stress, computed as

$$\sigma_{vM}^2 = \frac{1}{2}\left[\left(\sigma_{11}-\sigma_{22}\right)^2+\left(\sigma_{22}-\sigma_{33}\right)^2+\left(\sigma_{33}-\sigma_{11}\right)^2\right]+ 3\left(\sigma_{12}^2+\sigma_{23}^2+\sigma_{31}^2\right).$$

Nevertheless, this work is not restricted to this particular expression and the general formulation applies to any criterion that can be written as a function of the stress or strain tensor, defined generically as in (9).

Now it is necessary to define an appropriate failure criterion for the fictitious microstructure. A proposition was discussed by Duysinx and Bendsøe (1998) and the main features are summarized here. Homogenized stresses are related to homogenized deformations (brackets are used to emphasize homogenized average values), through (6), by

$$\langle\sigma(\mathbf{x})\rangle = \mathbf{D}_\rho\langle\varepsilon(\mathbf{x})\rangle = f_D(\rho)\,\mathbf{D}^0\langle\varepsilon(\mathbf{x})\rangle\,, \tag{10}$$

which is the relationship used in the equilibrium problem. However, local stresses within a cell are assumed to take values greater than the average value $\langle\sigma(\mathbf{x})\rangle$, say,

$$\sigma(\mathbf{x}) = \frac{1}{f_\sigma(\rho)}\langle\sigma(\mathbf{x})\rangle\,, \qquad 0 \le f_\sigma(\rho) \le 1\,. \tag{11}$$

Proposing that $f_D(\rho) = f_\sigma(\rho)$ and substituting (10) into (11), it is found that local stresses are related to homogenized deformations through the original (solid material) elasticity tensor:

$$\sigma(\mathbf{x}) = \mathbf{D}^0\langle\varepsilon(\mathbf{x})\rangle\,. \tag{12}$$

This relationship has important consequences for the behavior of the problem. It means that if homogenized deformations remain finite, local stresses (used in the failure criterion) also remain finite. On the other hand, when the density goes to zero, high deformations may occur due to the low stiffness and, large, although finite, local stresses are obtained, as shown in (12). As a consequence, local constraints saturate and lock the material-removal process. This is known as the *Stress Singularity Phenomenon*, initially found by Sved and Ginos (1968) in truss optimization problems. Later, Cheng and Jiang (1992) and Cheng and Guo (1997), showed the same event occurs in continuous problems. A frequent strategy adopted by many authors involves relaxing the stress constraints (Cheng and Guo 1997; Kirsch 1990), which allows stresses to take higher values when the density goes to zero and satisfies the original constraint for solid material. Then, constraints are transformed in

$$\begin{cases} g_\sigma(\mathbf{x}) \equiv \rho(\mathbf{x})\,F(\sigma(\mathbf{x})) - \epsilon(1-\rho(\mathbf{x})) \le 0\,, & \text{a.e. in } \Omega\,,\\ 0 < \epsilon^2 \le \rho_{\min} \le \rho(\mathbf{x}) \le 1\,, & \forall\,\mathbf{x}\in\Omega\,, \end{cases} \tag{13}$$

where ϵ is a relaxation parameter. Taking this proposition into consideration, the problem is rewritten as

Problem P_2 :

$$\underset{\rho\in K_\rho(\Omega)}{\text{Min}}\; m(\rho) = \rho_0\int_\Omega \rho(\mathbf{x})\,\mathrm{d}\Omega\,, \tag{14}$$

$$\text{Subject to}: g_\sigma(\mathbf{x}) \le 0 \quad \text{a.e. in } \Omega\,,$$

where $K_\rho(\Omega)$ is the design space of density fields:

$$K_\rho(\Omega) = \left\{\rho \mid \rho\in L^\infty(\Omega)\,,\; 0 < \epsilon^2 \le \rho_{\min} \le \rho(\mathbf{x}) \le 1\right\}.$$

3.2 Checkerboard regularization

Several alternatives to mitigate the checkerboard phenomenon are available in literature. A group of them are based on the idea of imposing appropriate constraints on the design set in order to obtain a closed subset and, consequently, turn the problem into a well-posed one. This can be done by imposing a local limit on the gradient components, computed as the difference in density between adjacent elements divided by the distance between them (Bendsøe 1995; Petersson and Sigmund 1998). Others are based on limiting the domain solution perimeter (Haber *et al.* 1995; Petersson 1999). A quite elegant solution is discussed by Borrvall and Petersson (2001). Using an isotropic microstructure approach, the volume of intermediate material is penalized by a functional. Proof of the existence of the solution is also shown. The present work uses a relatively different approach proposed by Pereira (2001), which introduces a limit for the gradient norm through penalization. A concomitant work of Borvall (2001) presents this strategy and a complete theoretical discussion about restrictions on the design space.

Thus, the new expression of the problem is the following:

$$\underset{\rho\in W^{1,2}(\Omega)}{\text{Min}}\; m(\rho) = \int_\Omega \rho\,\mathrm{d}\Omega \tag{15}$$

$$\text{Subject to}: \begin{cases} |\nabla\rho|^2_{L_2(\Omega)} \le C\,|\Omega|\,,\\ 0 < \rho_{\min} \le \rho(\mathbf{x}) \le 1\,,\\ g_\sigma(\mathbf{x}) \le 0 \quad \text{a.e. in } \Omega\,. \end{cases}$$

Clearly, problem (15) includes a single global constraint on the density gradient. Many procedures for solving problem (15) may be chosen. Considering penalization and a positive parameter r_ρ, the new objective functional can be written as

$$\underset{\rho\in W_{\rho}^{1,2}(\Omega)}{\text{Min}}\; m(\rho)=\int_{\Omega}\rho\;\mathrm{d}\Omega+\frac{1}{2}r_{\rho}\int_{\Omega}f_{\rho}(\rho)\;\mathrm{d}\Omega+$$

$$r_{m}\int_{\Omega}f_{m}(\rho)\;\mathrm{d}\Omega \tag{16}$$

$$\text{Subject to}: g_{\sigma}(\mathbf{x})\leq 0 \quad \text{a.e. in } \Omega\,,$$

$$\text{where } f_{\rho}(\rho)=(\nabla\rho)^{T}(\nabla\rho),\quad f_{m}(\rho)=\rho(1-\rho),\quad \text{and}$$

$$W_{\rho}^{1,2}(\Omega)=\left\{\rho\,|\,\rho\in W^{1,2}(\Omega)\,;\;0<\rho_{\min}\leq\rho(\mathbf{x})\leq 1\,,\right.$$
$$\left.\forall\,\mathbf{x}\in\Omega\right\}\,.$$

The function $f_m(\rho)$ in (16) is included in order to introduce an explicit penalization at the intermediate densities. Although different functions may be used, this one is chosen by many authors. The constant $r_m \geq 0$ is the associated penalization factor.

4
Solution by the augmented Lagrangian method

Due to its local nature, material failure constraints in (16) may be compared with plasticity-type constraints or unilateral contact constraints. Moreover, the Augmented Lagrangian (AL) technique has proven to be an efficient approach for solving the last type of problems. Initial computations show that the present formulation is very sensitive to stress constraints. Due to this, the augmented Lagrangian method was chosen in an effort to stabilize the optimization process through appropriate choices of penalization factors as well as schemes for updating Lagrangian multipliers. Following the classical procedure (Bertsekas 1996), the augmented Lagrangian functional is defined for this problem as

$$\begin{aligned}\pounds(\rho;\lambda,r)&=m(\rho)+m_{\sigma}(\rho;\lambda,r)\\&=m(\rho)+\int_{\Omega}M_{\sigma}(\rho;\lambda,r)\;\mathrm{d}\Omega\,,\end{aligned} \tag{17}$$

$$M_{\sigma}(\rho;\lambda,r)=$$

$$\frac{1}{r}\max\left\{g_{\sigma}(\rho,\sigma)\left[r\lambda+\frac{1}{2}g_{\sigma}(\rho,\sigma)\right]\;;\;-\frac{(r\lambda)^{2}}{2}\right\}, \tag{18}$$

where $\lambda\in L^2(\Omega)$ is a multiplier function and $r>0$ is the penalization parameter. This approach leads to a procedure based on a sequence of optimization subproblems; given a Lagrange multiplier field $\lambda^k\in L^2(\Omega)$ and a penalization factor $r^k>0$, the following box minimization problem is solved:

$$\underset{\rho\in W_{\rho}^{1,2}(\Omega)}{\text{Min}}\;\pounds\left(\rho;\lambda^{k},r^{k}\right). \tag{19}$$

Once this subproblem is solved, the Lagrange multiplier field λ^k as well as the penalization factor r^k are conveniently updated (Bertsekas 1996):

$$\lambda^{k+1}=\max\left\{\lambda^{k}+\frac{1}{2}g_{\sigma}(\rho,\sigma);0\right\}\,, \tag{20}$$

$$r^{k+1}=\frac{r^{k}}{t}\quad t>1\,. \tag{21}$$

5
Sensitivity analysis

Classical first-order optimization algorithms need information about functional values and their derivatives. In this case, the gradient of the objective functional (19) for fixed and known values of λ^k and r^k is needed. The functional $\pounds(\rho;\lambda,r)$ in (17) has two different terms. The first one, $m(\rho)$, depending only on the density field ρ and its derivative, is given straightforwardly by

$$\dot{m}(\rho)[y]=\int_{\Omega}\left[1+r_{m}\frac{df_{m}(\rho)}{d\rho}+\frac{1}{2}r_{\rho}\frac{df_{\rho}(\rho)}{d\rho}\right]y\;\mathrm{d}\Omega\,, \tag{22}$$

where y is a variation of ρ. On the other hand, the second term, $m_\sigma(\rho;\lambda,r)$, is implicitly dependent on ρ, and its derivative implies the differentiation of the stress field σ. To this end, continuum sensitivity analysis is used, in particular the adjoint method (Haug *et al.* 1986). Thus, the total Gateaux derivative of $m_\sigma\left(\rho;\lambda^k,r^k\right)$ for a direction y takes the from

$$\dot{m}_{\sigma}\left(\rho;\lambda^{k},r^{k}\right)[y]=$$

$$m'_{\sigma}\left(\rho;\lambda^{k},r^{k}\right)[y]-B'(\mathbf{u},\mathbf{u}_{a})[y]+l'(\mathbf{u}_{a})[y]\,, \tag{23}$$

where the notation $(\cdot)'[y]$ represents the partial (Gateaux) derivative of the functional $(\cdot)$ relative to the explicit dependence of ρ in direction y. All terms on the RHS. are evaluated at the current displacement $\mathbf{u}$ and at the adjoint solution $\mathbf{u}_a$ related to the adjoint problem discussed next in Sect. 5.1.

The first term on the RHS of (23) consists basically of the partial derivative of the function $g_\sigma(\rho,\sigma)$ in (18), keeping σ fixed. Thus, considering (13) and the symbol $\langle(\cdot)\rangle^{+}=\max[(\cdot)\,;0]$, we have

$$\begin{aligned}\frac{\partial g_{\sigma}(\rho,\sigma)}{\partial\rho}\,y&=\frac{\partial}{\partial\rho}\left[\rho F(\sigma)+\epsilon(\rho-1)\right]\,y\\&=\left[F(\sigma)+\epsilon\right]\,y\,,\end{aligned} \tag{24}$$

and then,

$$m'_{\sigma}\left(\rho;\lambda^{k},r^{k}\right)[y]=\int_{\Omega}\frac{\partial M_{\sigma}\left(\rho;\lambda^{k},r^{k}\right)}{\partial\rho}\,y\;\mathrm{d}\Omega=$$

$$\int_{\Omega}\left\{\frac{1}{r^{k}}\left[F(\sigma)+\epsilon\right]\left\langle g_{\sigma}(\rho,\sigma)+r^{k}\lambda^{k}\right\rangle^{+}\right\}\,y\;\mathrm{d}\Omega\,. \tag{25}$$

The second term on the RHS of (23) is given by the partial (Gateaux) derivative of B, considering real displacements $\mathbf{u}$ and adjoint solution $\mathbf{u}_a$ fixed:

$$B'\left(\mathbf{u},\mathbf{u}_a\right)[y]=\lim_{t\to 0}\left[\frac{B_{\rho+ty}\left(\mathbf{u},\mathbf{u}_a\right)-B_{\rho}\left(\mathbf{u},\mathbf{u}_a\right)}{t}\right]=$$

$$\left[\frac{d}{dt}\int_{\Omega} f_D(\rho+ty)\left[D_0\left(\nabla^S\mathbf{u}\right)\cdot\left(\nabla^S\mathbf{u}_a\right)\right]\,\mathrm{d}\Omega\right]_{t=0}=$$

$$\int_{\Omega} q\rho^{(q-1)}\left[\sigma_0\cdot\nabla^S\mathbf{u}_a\right]\;y\;\mathrm{d}\Omega\,, \tag{26}$$

where the last expression is obtained from (5): $f_D(\rho)=\rho^q$ and the notation $\sigma_0\equiv D_0\nabla^S\mathbf{u}$ is used. It is worth emphasizing that, once the fields $\mathbf{u}$ and $\mathbf{u}_a$ are obtained, (26) allows the computation of the partial derivative of B through a simple integration over the subdomain defined by the support of the variation function $y\in W^{1,2}_{\rho}(\Omega)$, usually associated with a small groups of elements.

If it is assumed (for simplicity sake) that external loads do not depend on the density distribution (no body forces are considered), then the third term on the RHS of (23) is null.

Finally, the total derivative of m_σ is obtained by substituting (25) and (26) into (23). The next paragraphs are dedicated to detailing the evaluation of the adjoint solution $\mathbf{u}_a$.

5.1 Adjoint problem

In the general case, the second and third terms on the RHS of (23) depend on the solution $\mathbf{u}_a$ of the following adjoint variational problem:

Find $\mathbf{u}_a\in V$*, such that*

$$B\left(\mathbf{u}_a,\mathbf{v}\right)=\int_{\Omega}\left(\frac{\partial M_\sigma}{\partial\nabla^S\mathbf{u}}\,\nabla^S\mathbf{v}\right)\mathrm{d}\Omega\,,\quad\forall\,\mathbf{v}\in V\,. \tag{27}$$

The function M_σ in (18) depends on the stress field σ and, consequently, on the linear deformation tensor $\nabla^S\mathbf{u}$. Its derivative in (27) is obtained as

$$\frac{\partial M_\sigma}{\partial\nabla^S\mathbf{u}}=\frac{1}{r^k}\frac{\partial g_\sigma\left(\rho,\sigma\right)}{\partial\nabla^S\mathbf{u}}\left\langle g_\sigma\left(\mathbf{x}\right)+r^k\lambda^k\right\rangle^{+}\,. \tag{28}$$

Appendix A shows that the derivative of g_σ may be written as (A.5)

$$\frac{\partial g_\epsilon\left(\rho,\sigma\right)}{\partial\nabla^S\mathbf{u}}=\rho H^\sigma\,, \tag{29}$$

where H^σ is a second-order tensor obtained explicitly from the material failure criterion evaluated at the current stress state σ. Then, the final expression of the derivative of M_σ is

$$\frac{\partial M_\sigma}{\partial\nabla^S\mathbf{u}}=\frac{\rho}{r^k}\left\langle g_\sigma\left(\mathbf{x}\right)+r^k\lambda^k\right\rangle^{+}H^\sigma\,. \tag{30}$$

It is important to emphasize that, for a given stress state, the directional derivative of M_σ is computed using the same expression for any differentiable material failure function, with the only exceptions being the scalars B_1, B_2, and B_3 (Appendix A), which are explicitly dependent on the failure function $F(\sigma)$. A simple substitution of this last derivative into (27) completes the load term of the variational adjoint problem. Moreover, the bilinear form $B_\rho(\cdot,\cdot)$ is the same as that of the physical problem and, consequently, the numerical solution of $\mathbf{u}_a$ uses the same stiffness matrix as the one used to obtain $\mathbf{u}$.

6 Discretization

Although the proposed approach has no theoretical limitations for 3D problems, numerical tests were initially performed in two dimensions.

Different element types may be used to solve the boundary value problem. Most works use equal-sized quadrilateral elements due to the computational savings, since the element stiffness matrix is partially calculated only once. Higher order elements result in better performance for the checkerboard phenomenon but the computational cost increases. Discontinuous density fields are also a frequent choice in literature.

In this work, the three-node Lagrangian element was used to solve the boundary value problem as well as to define a continuous density field controlled by nodal parameters, which play the role of design variables here. This choice was guided by the double purpose of having a smoother boundary representation than that with quadrilateral elements as well as a mesh refinement flexibility if needed. Several other elements were tested, even higher orders elements, in order to stabilize the checkerboard. However all of them were much more expensive and inefficient when compared with the simple penalization functional. It must be noticed that the number of elements in linear-triangle meshes is about twice the number of nodes. Thus, nodal design variables represent half the number of element design variables. Furthermore, a continuous density field is in accordance with the formulation proposed.

Numerical integration was performed with only one integration point at the center of the triangle, the same place where stresses and the failure criterion were evaluated.

To complete this section it is important to summarize the main characteristics of the present proposal: The number of design variables equals the number of nodes and, consequently, the number of side constraints associated to design variables is twice the number of nodes. Finally, the number of stress constraints is equal to the number of elements.

7
Numerical algorithm

The numerical solution of the problem follows the regular procedure of the augmented Lagrangian method and it is executed in two stages. The first one is the external loop, in which each iteration consists of defining a Lagrange multiplier vector λ^k, a penalization factor for stress constraints r^k and solving the minimization of the objective functional $\mathcal{L}\left(\rho; \lambda^k, r^k\right)$ subject to side constraints, $\rho \in \mathcal{D}$, $\mathcal{D} = \{\rho \in \Re^n \mid 0 < \rho_{\min} \leq \rho_i \leq 1\}$. These steps are listed below:

External Loop

1. Define $k = 0,\ \eta^k,\ r_m,\ \ r_\rho,\ \ \lambda^k$ and r^k;
2. Minimize the functional $\mathcal{L}\left(\rho; \lambda^k, r^k\right),\ \rho \in \mathcal{D}$;
3. Verify convergence within a tolerance η^k;
4. Update η^k, λ^k and r^k;
5. $k = k+1,$ Return to Step 2.

The second stage is the internal problem 2 in which the functional $\mathcal{L}$ is minimized for fixed values of λ^k, r^k:

$$\min_{\rho \in \mathcal{D}} \ \mathcal{L}(\rho)\,. \tag{31}$$

To solve this problem a nonlinear trust-region algorithm proposed by Friedlander *et al.* (1994) and generalized by Bielschowsky *et al.* (1997) is used. We present here the outline of the algorithm, but a complete description is found in the references given. The algorithm is based on the minimization, at each inner iteration j, of a quadratic subproblem Q^j defined on a trust-region of size Δ^j:

$$Q^j(s) = \mathcal{L}(\rho^j) + s^T \nabla \mathcal{L}(\rho^j) + \frac{1}{2} s^T B^j s\,, \quad s = \rho - \rho^j\,,$$

$$s^j = \arg \min_{s \in \Re^n} \{Q^j(s) \mid \left(\rho^j + s\right) \in \mathcal{D} \text{ and } \|s\| \leq \Delta^j\}\,,$$

where $B^j \in \Re^{n \times n}$ is an approximation of $\nabla^2 \mathcal{L}(\rho^j)$. An adaptive strategy based on the quality of the approximated subproblem that modifies the size of the trust region to accelerate convergence is also used. To this end, the quotient μ^j is computed using

$$\mu^j = \frac{\mathcal{L}(\rho^j) - \mathcal{L}(\rho^j + s^j)}{Q_k(0) - Q_k(\rho^j)}\,. \tag{32}$$

If μ^j is near unity, it means that the quadratic function is a good approximation within the box limits Δ^j and the box may be increased. Otherwise, it should be reduced. The basic algorithm of the trust region can be written as follows:

Internal Loop

1. Define $Delta^j \in (0, \Delta_{\max})\,,\ \ B^j \in \Re^{n \times n},\ \ \rho^j \in \mathcal{D}$;
2. Define the Quadratic Subproblem (QS):
   $Q^j(s) = \mathcal{L}(\rho^j) + s^T \nabla \mathcal{L}(\rho^j) + \frac{1}{2} s^T B^j s$;
3. Minimize the QS:
   $s^j = \arg \min_{s \in \Re^n} \{Q^j(s) \mid \left(\rho^j + s\right) \in \mathcal{D}\,,\ \|s\| \leq \Delta^j\}$;
4. Compute quotient μ^j;
5. Compute the new trust region size Δ^j:
   a. If $\mu^j < \frac{1}{4}$, then $\Delta^{j+1} = \frac{1}{4}\Delta^j$;
   b. if $\frac{1}{4} \leq \mu^j \leq \frac{3}{4}$, then $\Delta^{j+1} = \Delta^j$;
   c. if $\mu^j > \frac{3}{4}$, then $\Delta^{j+1}\ \min\left(2\Delta_k,\ \Delta_{\max}\right)$;
6. Update the design:
   a. if $\mu^j > \bar{\mu}$, then $\rho^{j+1} = \rho^j + s^j$;
   b. if $\mu^j \leq \bar{\mu}$, then $\rho^{j+1} = \rho^j$;
7. $j = j+1$, Return to Step 2.

In order to solve the minimization of a quadratic function within the box constraints in Step 3, an active set algorithm is used, which generates a sequence of points on a face of the polytope until a minimizer of the objective function on that face or a point on the boundary is reached. In the first case the iteration is allowed to leave the current face and the algorithm continues working on a face of higher dimension. The present results were obtained with an implementation of this algorithm, called BOX-QUACAN, parametrically adapted to this problem.

8
Numerical results

In order to analyze the performance of the proposed approach, several examples are shown. Many of them present comparisons between the present approach and the classical compliance approach (Bendsøe and Kikuchi 1988). In the last case, stress constraints are substituted by a unique mass constraint.

Before detailing each example, it is worth commenting on the influence of parameters like η^k, r_m, r_ρ, λ^k and r^k on the numerical results.

The penalization of the checkerboard parameter r_ρ has a strong influence on the topological complexity. This fact is clearly seen in the example in Sect. 8.3, in which different values of r_ρ were used. The bigger the parameter the simpler the topology with a rough boundary definition obtained. Moreover, it was noted that very small values of r_ρ were enough to prevent the checkerboard phenomenon. Most of the examples were run with $r_\rho = 0.001$. The parameter r_m is used to penalize intermediate densities. If we require the penalized density function $\rho + r_m f_m(\rho)$ to have a negative derivative for every ρ, the value of r_m must be less than unity. Most of the examples were run with $r_m = 0.95$. In spite of this, it was noted that the influence of this parameter is smaller than that of r_ρ or ϵ. The penalization of the stress constraint r^k changes at each iteration of the augmented Lagrangian sequence. In the present implementation, it goes from $r^k = 1$ to a lower limit of $r^k = 10^{-4}$ (note in (13) that penalization is proportional to the inverse of r^k). The Lagrangian multiplier λ^k is automatically updated by the algorithm.

Cheng and Guo (1998) state a limit of $\epsilon^2 \leq \rho_{min}$ in order to avoid singular points. Most of the examples here were run with $\epsilon^2 = \rho_{min} = 0.01$. As the elasticity tensor is proportional to ρ^3, the Young modulus for a minimum density is 10^{-6} times smaller than that for a solid material. The example in Sect. 8.2 shows the influence of ϵ on the results. The behavior is in accordance with the nature of this parameter: the constraints are weakened for positive values of epsilon. Thus, more robust designs are obtained for smaller values of ϵ and vice versa. Moreover, convergence is easier for greater values of ϵ. Finally, η^k represents the tolerance for convergence in the external loop of the augmented Lagrangian. The variation of the objective function, the step-size and satisfaction of stress constraints are tested. Convergence occurs if

$$\left\|\rho^{k+1} - \rho^k\right\| \leq 10^{-3}\sqrt{n}$$

and

$$\left|\pounds\left(\rho^{k+1}; \lambda^{k+1}, r^{k+1}\right) - \pounds\left(\rho^k; \lambda^k, r^k\right)\right| \leq 10^{-4}\left\|\Omega\right\| ,$$

where n is the number of design variables and $\|\Omega\| = meas(\Omega)$.

Most computations converged within the range of 30 to 90 augmented Lagrangian iterations. However, the last $\frac{3}{4}$ of the total iterations were dedicated the "fine-tuning", in which stress constraints are satisfied.

8.1
Bar in traction and flexion

This example discusses the case of a bar that is submitted to two different loads: a simple traction and a bending moment due to a linear distribution of stress along the right vertical boundary (see Fig. 2). The domain is decomposed in two regions. The right side is fixed, while the left one is optimized.

For the first case, the traction is set to $t = 30\,\text{Pa}$ while $\sigma_{adm} = 60\,\text{Pa}$. Symmetry conditions are used. The mesh has 1510 nodes and 2868 elements. The optimal solution has, on its left side, the design of a bar whose transverse section is half the size of the original one and it is fully stressed, as expected (Figs. 4 and 5). The design of the right side is enforced to follows the flux of stresses due to the traction along the complete unmodified section. This transition is clearly not fully stressed.

The second load case is a distribution of normal stress from $t = 30\,\text{Pa}$ at the bottom line to $t = -30\,\text{Pa}$ at the top line. A minimum mass problem is run subject to a $\sigma_{adm} = 35\,\text{Pa}$. Figure 6 shows the final design in which the material is concentrated at the "flanges" as expected. Figures 7 and 8 show the ϵ-relaxed failure function and σ_x distribution respectively. It is possible to see that the constraints are satisfied within a small error. However, saturation only occurs for the top and bottom lines of the solid body. Figure 8 clearly shows that the stresses σ_x go from a maximum value at the bottom of 35 Pa to -35 Pa

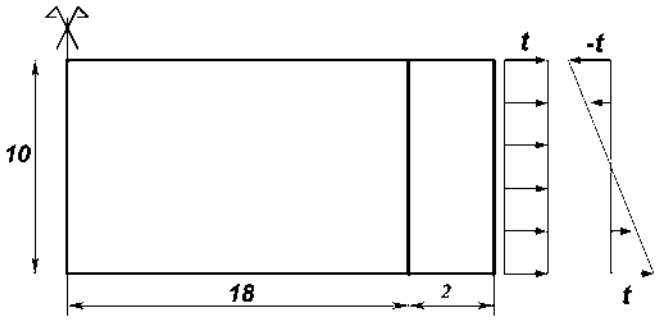

Fig. 2 Bar in traction and flexion

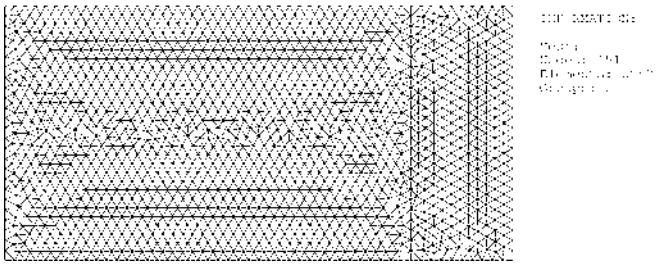

Fig. 3 Bar in traction and flexion: FEM mesh

Fig. 4 Traction load case: final density

Fig. 5 Traction load case: ϵ-relaxed failure function

Fig. 6 Bending load case: final density

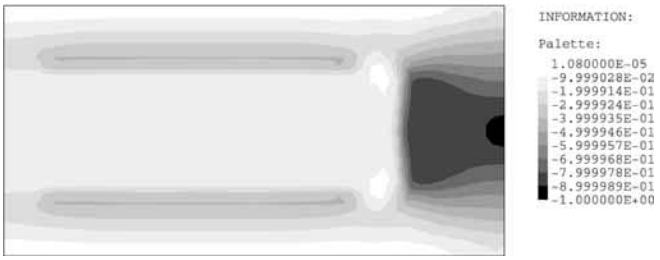

Fig. 7 Bending load case: ϵ-relaxed failure function

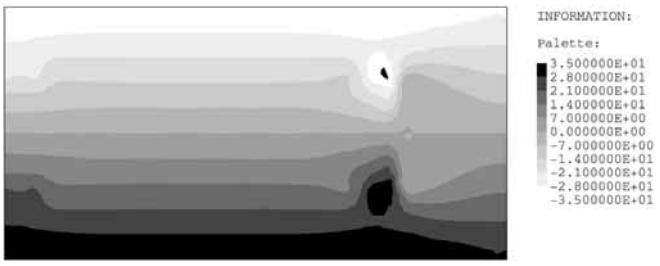

Fig. 8 Bending load case. Stress component σ_x

at the top. Further elimination of material, even in non-saturated regions will produce a violation of constraints elsewhere. In other words, the local minimum obtained does not satisfy the fully-stressed design conditions. The material and geometric parameters were the following:
$E = 100.0\,\text{Pa}$; $\nu = 0.3$; $t = 30.0\,\text{Pa}$.

8.2 L-shaped domain

This example investigates the behavior of the proposed approach in an initial domain containing a stress singularity. Figure 9 shows the model clamped on its top boundary and loaded by a vertical resultant force P. The initial parameters were the following:
$E = 100\,\text{Pa}$; $\nu = 0.3$; $\sigma_{adm} = 42.42\,\text{Pa}$; $L = 1.0\,\text{m}$; $r_\rho = 0.001\,\text{m}^2$; $r_m = 0.95$; $P = 1.0\,\text{N}$.

The mesh is properly refined on the singular vertex (Fig. 10) having 2722 nodes and 5218 elements. Three different cases were run to verify the influence of the relaxation parameter on results: $\epsilon = 1.0,\ 0.1,\ 0.05$. The final designs for each case are shown in Figs. 11, 12 and 13. It is possible to see that better-defined and more robust designs are obtained for smaller values of ϵ, which is in accordance with the characteristic of ϵ: high values of ϵ allow high values of stresses at intermediate densities and consequently lighter designs are obtained. Moreover, the rounded boundary on the singular corner becomes more accentuated as ϵ decreases and makes this point more sensitive to high stresses.

The minimum compliance was also computed. In order to make it comparable with previous results, the final mass for $\epsilon = 0.1$ was used as the upper bound for the minimum compliance approach. The final design is shown

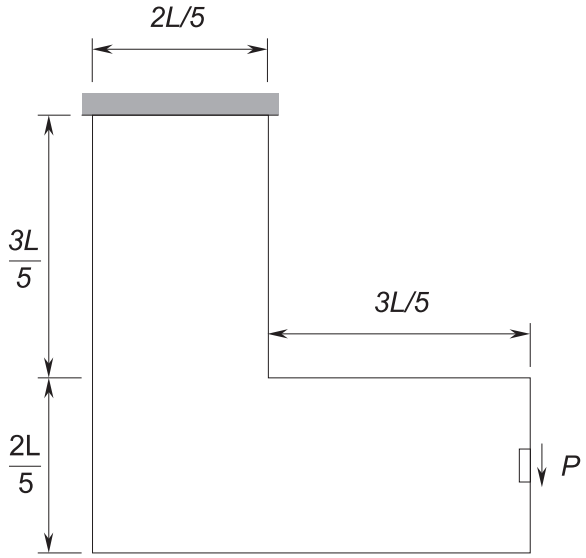

Fig. 9 L-shaped domain: model

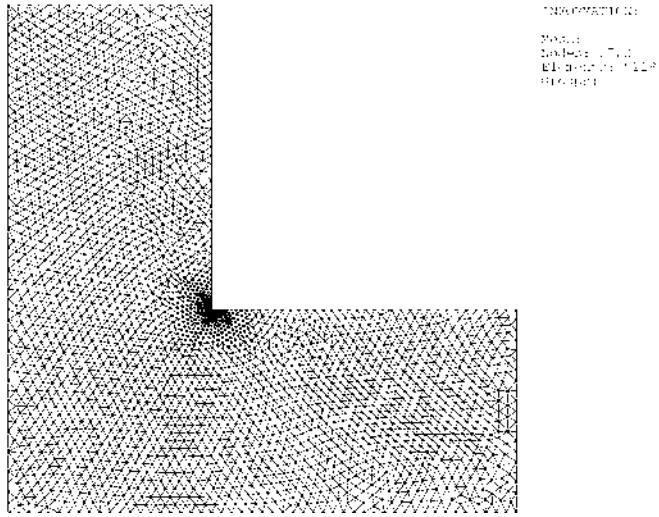

Fig. 10 L-shaped domain: FEM mesh

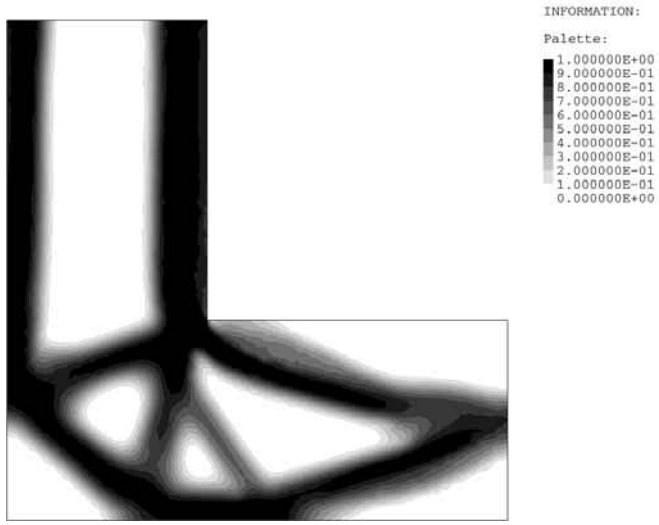

Fig. 11 Minimum mass approach: final density for $\epsilon = 1.0$

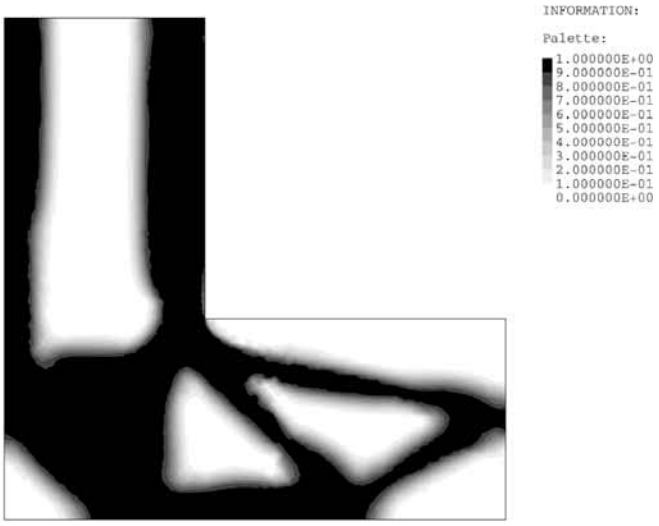

Fig. 12 Minimum mass approach: final density for $\epsilon = 0.1$

Fig. 13 Minimum mass approach: final density for $\epsilon = 0.05$

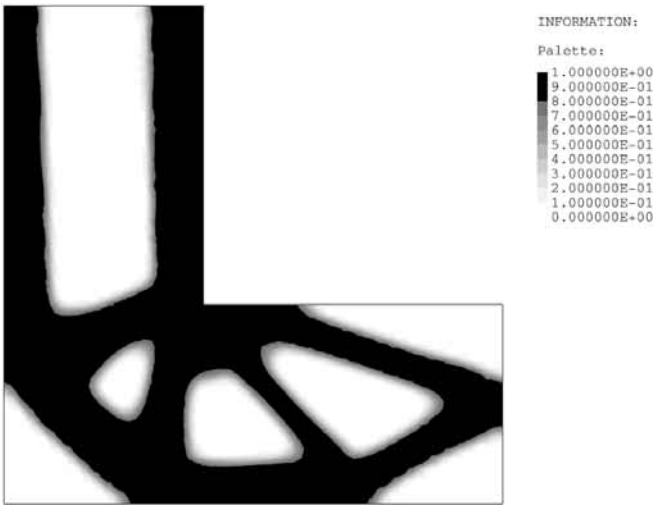

Fig. 14 Minimum compliance approach

in Fig. 14. It is possible to see that the minimum mass formulation is able to capture localized stresses and also to avoid high stress concentrations with a well-defined rounded boundary on the singular corner. On the other hand, the compliance formulation seeks the maximum transverse section in order to obtain maximum stiffness, no matter how much the stress values rise. Figures 15 and 16 show the ϵ-relaxed failure constraint for both cases, and Table 1 gives a summary of final values for

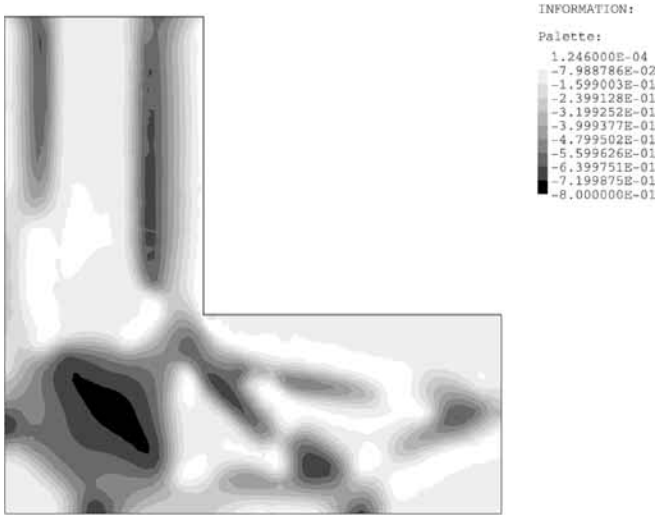

Fig. 15 Minimum mass approach: ϵ-relaxed failure function for $\epsilon = 0.1$

Fig. 16 Minimum compliance approach: ϵ-relaxed failure function

Table 1 Comparison of formulations

Approach	$F_\rho(\rho)$	Mass	Compl. (Nm)	Time (min)
Mass	0.0903	0.3608	2.0374	100
Compliance	0.1189	0.3608	1.6571	15

mass, compliance and computational times. This problem has already been investigated by Duysinx and Bendsøe (1998) and the final designs are comparable to the present ones. However, rougher meshes were used and the singularity could not be properly captured.

8.3 MBB-beam

The *MBB-beam* (Messerschmitt-Bolkow-Blohm GmbH; Payten *et al.* 1998; Bulman *et al.* 2001) is one of the classic benchmarks of topology optimization. It consists of a simply supported beam, loaded with a vertical force centered on its top boundary (Fig. 17). The inital parameters were the following:
$E = 21\,\text{MPa};\ \nu = 0.3;\ \sigma_{adm} = 17.8\,\text{kPa};$
$L = 1.0\,\text{m};\ \Delta L = 0.2\,\text{m};\ r_\rho = 0.002\,\text{m}^2;$
$r_m = 0.95;\ P = 2.0\,\text{kN}.$

Due to symmetry conditions, only half of the domain is meshed with 2923 nodes and 5614 elements (Fig. 18). Once again, both formulations, minimum mass and minimum compliance were tested. The final mass obtained with the first formulation was used as the upper bound in the mass constraint of the compliance problem. The final designs are shown in Figs. 19 and 20, while the ϵ-relaxed failure distributions are given in Figs. 21 and 22. Some remarks can be made from the analysis of those figures. It is possible to see that identical topologies were obtained, but the shapes and sections of the internal bars are quite different. It is also possible to see that the boundaries of the minimum mass solution present more "gray" regions than those from the compliance result. Moreover, these gray regions usually appear near junctions, in an effort to alleviate stress concentrations. On the other hand, the compliance solution give failure stresses of up to 70 % higher than the admissible value, while the minimum mass solution shows numerical errors only $0,012\%$ higher than the admissible value.

In order to perform the sensitivity analysis of the penalization functional for the checkerboard phenomenon, the same problem and a new refined mesh with 5159 nodes and 10 010 elements were used (Fig. 23). Three different values of the penalization factor were tested: $r_\rho = 0.0001$, $r_\rho = 0.001$ and $r_\rho = 0.01$. Figures 24, 25 and 26 show the final results for the minimum mass approach, while Figs. 27, 28 and 29 show the solutions for the com-

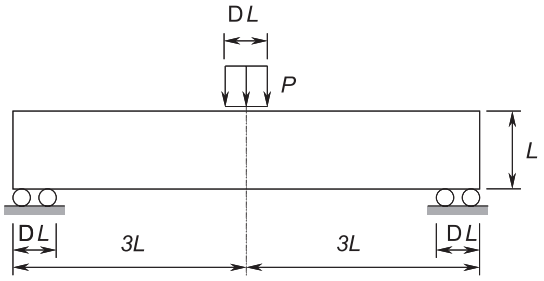

Fig. 17 MBB-beam: model

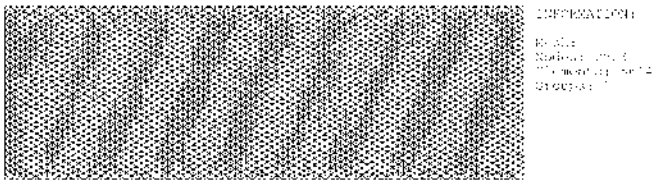

Fig. 18 MBB-beam: FEM mesh

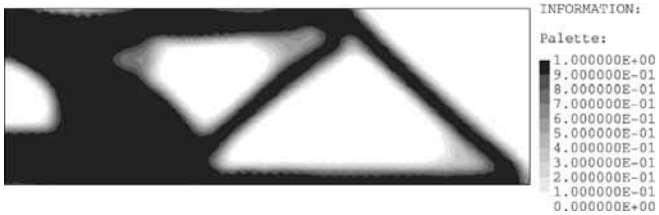

Fig. 19 Minimum mass approach: final density

Fig. 20 Minimum compliance approach: final density

Fig. 21 Minimum mass approach: ϵ-relaxed failure function

Fig. 22 Minimum compliance approach: ϵ-relaxed failure function

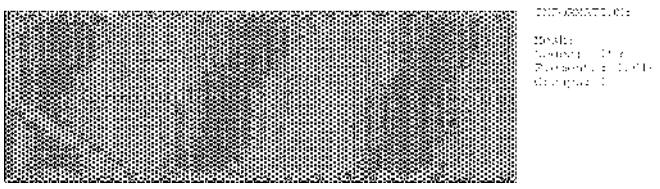

Fig. 23 MBB-beam: refined mesh

pliance approach. Table 2 summarizes the final results for each case. It can clearly be seen that there is a strong dependence of the final topology on this parameter. As expected, low values of penalization lead to a complex final topology together with a clean boundary definition. Opposite to this, simpler topologies and wide gray regions

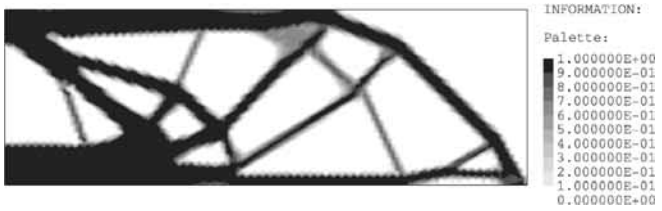

Fig. 24 Minimum mass approach: final density for $r_\rho = 0.0001$

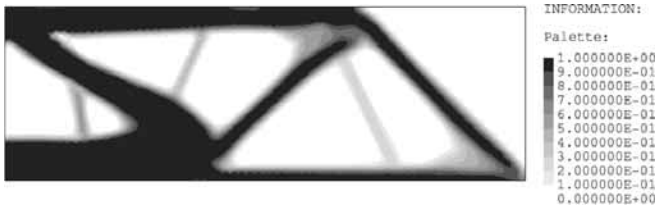

Fig. 25 Minimum mass approach: final density for $r_\rho = 0.001$

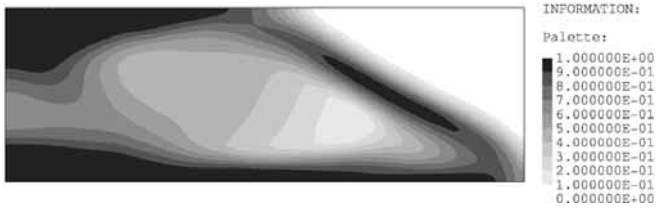

Fig. 26 Minimum mass approach: final density for $r_\rho = 0.01$

Fig. 27 Minimum compliance approach: final density for $r_\rho = 0.0001$

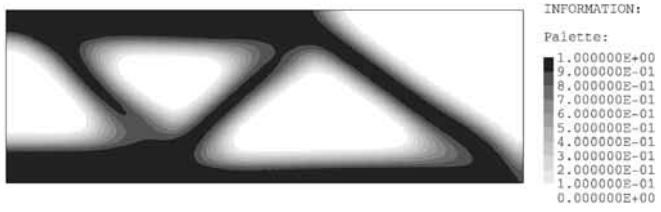

Fig. 28 Minimum compliance approach: final density for $r_\rho = 0.001$

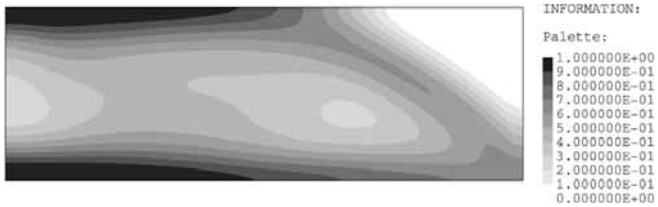

Fig. 29 Minimum compliance approach: final density for $r_\rho = 0.01$

Table 2 MBB-beam: Sensitivity analysis of factor r_ρ

Approach	r_ρ	Mass	Compl. (Nm)	Time (min)
Mass	0.0001	1.2172	2.3795	410
Mass	0.0010	1.2691	2.3771	336
Mass	0.0100	1.6621	2.3280	240
Compliance	0.010	1.5000	1.7642	180
Compliance	0.100	1.5000	2.0151	150
Compliance	1.000	1.5000	3.0762	52

are obtained for higher values of r_ρ, which is even capable of making the design invalid (as can be seen for $r_\rho = 0.01$). It is also clear that simpler designs are associated with lower computational times.

8.4 Michell's structure

This is another classic case in topology compliance optimization. It was proposed by A.G.M. Michell (Michell 1904). It consists of a plate with clamping conditions on an internal circular boundary and loaded by a vertical force P on its right boundary (Figure 30 shows the mechanical problem). The present example has as a goal the emphasis of the checkerboard phenomenon in the minimum mass approach using a SIMP material. Two cases were tested; first, no penalization was used ($r_\rho = 0.0$) and second, a penalization factor of $r_\rho = 0.03\,\mathrm{mm}^2$

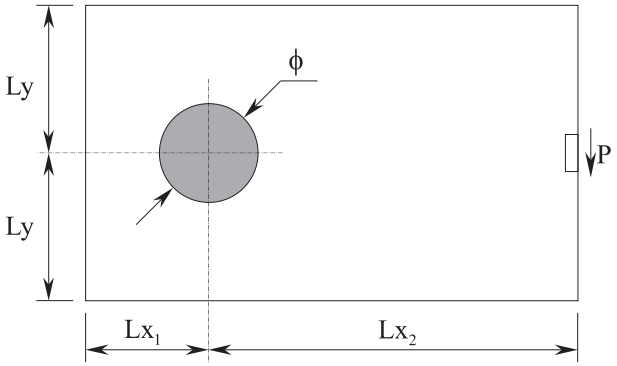

Fig. 30 Michell 's problem: model

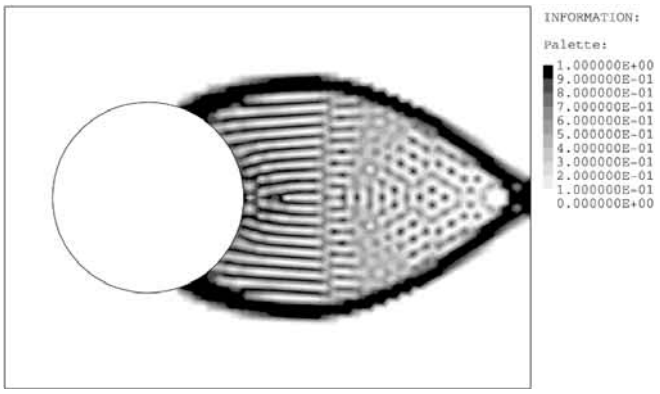

Fig. 31 Final density for $r_\rho = 0.0$

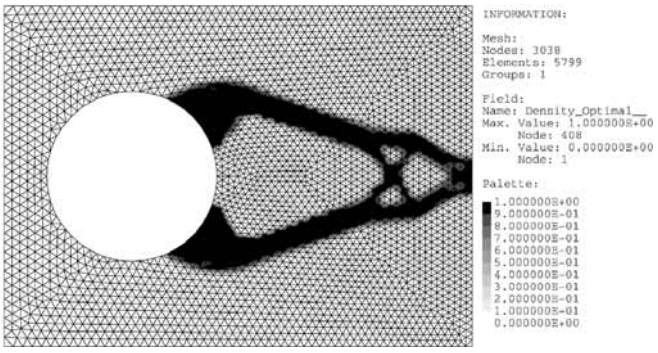

Fig. 32 Final density for $r_\rho = 0.03$

was included. The initial operating parameters were the following:

$E = 100.0\,\mathrm{N/mm^2}$; $\nu = 0.3$; $\sigma_{adm} = 0.60\,\mathrm{N/mm^2}$
$P = 1.0\,\mathrm{N}$; $Lx_1 = 15\,\mathrm{mm}$; $Lx_2 = 40\,\mathrm{mm}$; $Ly = 40\,\mathrm{mm}$;
$\phi = 20\,\mathrm{mm}$; $r_m = 0.95$.
A mesh of 3038 nodes and 5799 elements was chosen. If no regularization is included, a clear checkerboard appears (Fig. 31). On the other hand, Fig. 32 shows the solution for $r_\rho = 0.03$.

8.5 Anisotropic failure criterion

This example discusses results obtained when an anisotropic failure criterion is used. The mechanical case is shown in Fig. 33, in which a rectangular plate is submitted to a shear force at its bottom boundary while it is clamped on its top boundary. A mesh of 2222 nodes and 4242 elements gives the initial domain (Fig. 34). The problem was solved with the Raghava criterion (Raghava *et al.* 1973) with a quotient between the admissible values of compression and traction of $s = \sigma_{comp}/\sigma_{tra} = 3.0$. The final density distribution, ϵ-relaxed failure function and the failure function itself are show in Figs. 35, 36 and 37 respectively. It is clear that the bar submitted to traction is the one with the thicker final design. On the other hand, a *fully stressed design* was not reached; the right bar is submitted to a stress level lower than admissible, while the left one is completely saturated. This is a clear case in which stiffness is needed in **one** region of the structure in order to avoid material failure in the **other** region. One must note that this case is not equivalent to that of two 1D-bars because of the clamped nodes and fixed thick-

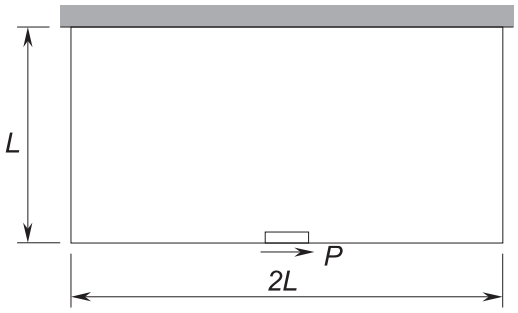

Fig. 33 Anisotropic failure criterion: model

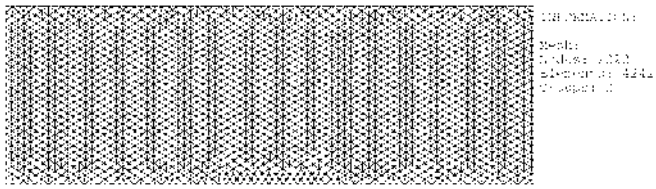

Fig. 34 Anisotropic failure criterion: FEM mesh

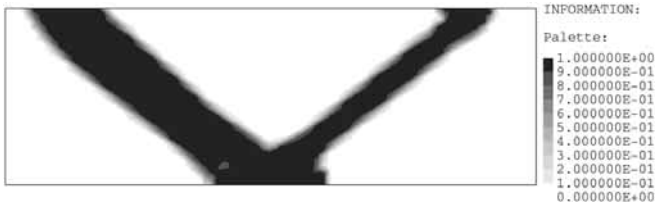

Fig. 35 Final density field

Fig. 36 ϵ-relaxed failure function

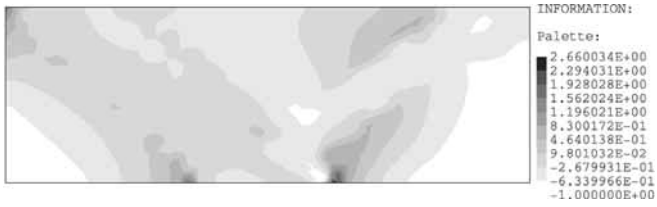

Fig. 37 Failure function without relaxation

ness. The left bar is submitted to traction and bending efforts simultaneously and its behavior is similar to that of the first example: outer fibers of the left bar are more tractioned (saturated) than inner fibers (not saturated). Thus, the local minimum obtained indicates that it is more convenient to maintain an unsaturated thin right bar than using more material on the left bar to support bending stresses.

Another important issue is the difference between the ϵ-relaxed constraint (Fig. 36) and the constraint without relaxation (Fig. 37). Real failure is reached at points with almost no material, which is in accordance with the formulation. The operational parameters were the following:

$E = 100.0\,\mathrm{N/m^2};\ \nu = 0.3;\ L = 1.0\,\mathrm{m};$

$P = 1.0\,\mathrm{N};\ \sigma_{tra} = 2.5\,\mathrm{N/m^2};\ \sigma_{comp} = 7.5\,\mathrm{N/m^2};$

$s = \dfrac{\sigma_{comp}}{\sigma_{tra}} = 3.0;\ r_m = 0.80;\ r_\rho = 0.001\,\mathrm{m^2}.$

8.6 Eye-bar

This last example deals with a practical problem of finding the optimal design for an eye-bar belonging to an eye-bar-chain of a suspended bridge (see Fig. 38). The mechanical problem and mesh are sketched in Figs. 39 and 40. A distributed pressure t_n whose value depends on the coordinate θ is applied on the internal surface of the eye:

$$t_n(\theta) = 2\,p_{máx} \begin{cases} \dfrac{\theta}{\pi}, & \text{if } 0 \le \theta \le \dfrac{\pi}{2}, \\ 1 - \dfrac{\theta}{\pi}, & \text{if } \dfrac{\pi}{2} < \theta \le \pi. \end{cases}$$

The operating parameters were:

$E = 210\,000\,\mathrm{MPa};\ \nu = 0.3;\ r_m = 0.95;$
$r_\rho = 0.001\,\mathrm{mm^2};\ L_x = 800\,\mathrm{mm};\ L_y = 1651\,\mathrm{mm};$

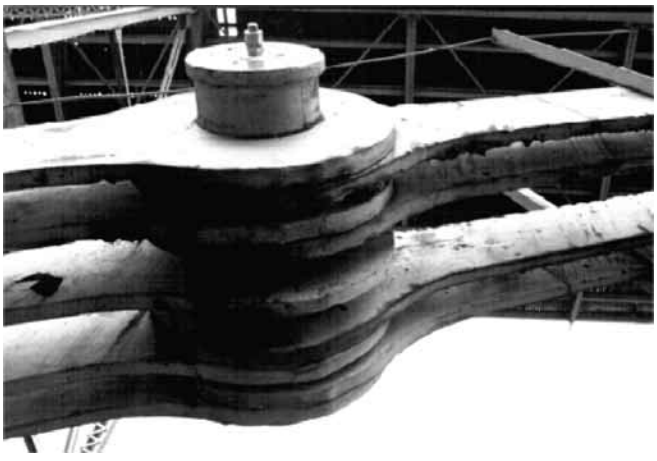

Fig. 38 Eye bar chain of Hercilio Luz bridge in Florianópolis, Brazil

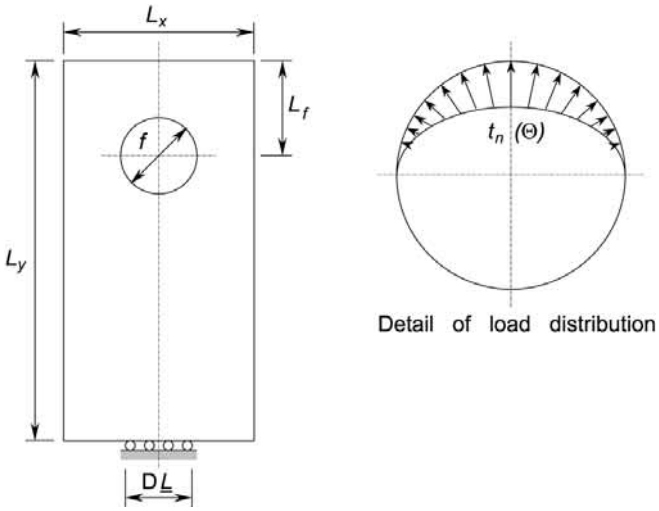

Fig. 39 Eye-bar: model

$L_\phi = 451\,\mathrm{mm};\ \Delta L = 254\,\mathrm{mm};\ \phi = 292\,\mathrm{mm};$
$h = 50.8\,\mathrm{mm};\ p_{máx} = 21\,802\,\mathrm{MPa};\ \sigma_{adm} = 440\,\mathrm{MPa}.$

Due to symmetry conditions, only half of the geometry is meshed with 2395 nodes and 4546 elements. The solution is obtained with a mass reduction of 63.33% (Fig. 41). Final design is not likely to be easily foreseen by mechanical intuitive process. In order to avoid bending stresses, the transverse section at both sides of the hole is smaller than at the symmetry plane, while an horizontal bar helps to avoid bending. The ϵ-relaxed failure function remains below zero within numerical error. (Fig. 42).

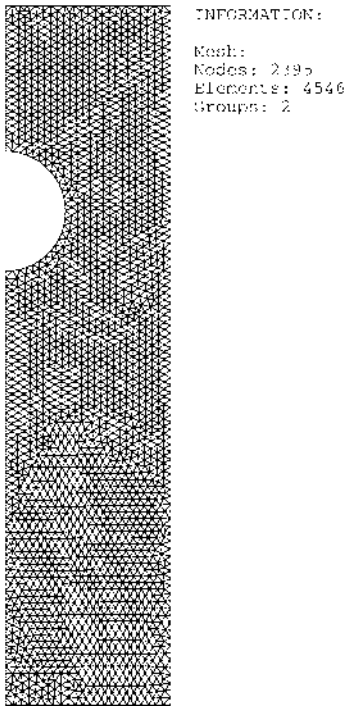

Fig. 40 Eye-bar: mesh

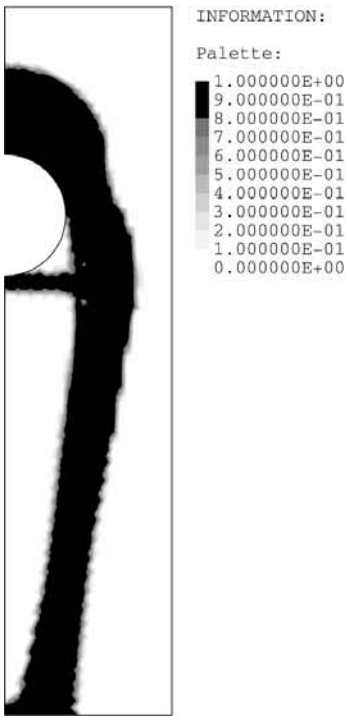

Fig. 41 Final density field

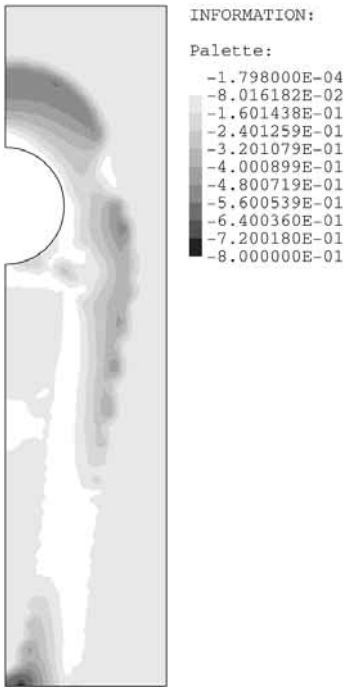

Fig. 42 ϵ-relaxed failure function

9 Concluding remarks

This work shows a formulation for the topological optimization of structures. The objective is the minimization of the mass constrained by a material failure criterion.

The SIMP approach is chosen and a continuous density field is used as the design variable. The material failure constraint field is numerically treated by an augmented Lagrangian algorithm associated with a Lagrange multiplier vector whose dimension is equal to the number of integration points over the domain (in the present implementation, stress evaluation points coincide with the integration points at each element). Within this approach, gradient computation is obtained at the simple cost of a back substitution and domain integration. Some concluding remarks may be drawn from this experience:

1. Final designs with good geometric representations were obtained, in general with small gray regions, which facilitates post-processing operations.
2. The failure ϵ-relaxed criterion is (numerically) satisfied everywhere in the mesh, and final designs show smooth boundaries, therefore avoiding stress concentrations.
3. Beginning with identical initial conditions and using the same final mass, the stress-based formulation drives to quite different designs to those obtained with the compliance formulation.
4. The stress formulation is associated with a computational effort up to 10 times greater than the effort expended for the compliance problem. The first reason is the great difference in the nature and in the number of constraints of both problems. Despite this, reasonably low computational times were obtained on simple personal computers, which encourages further applications.
5. The checkerboard phenomenon also appears in the present formulation based on the SIMP approach. However, the procedure used, based on a simple penalization function associated with the gradient of the density field, is found to be an efficient and low cost inhibitor of the checkerboard phenomenon.
6. As $\rho_{\min}$ always remains greater than zero during the whole mathematical programming process, the stress singularity phenomenon is still a strong challenge, even with the use of ϵ-relaxed constraints.

Finally, it is worth mentioning that a formulation based on the concept of a pointwise material failure constraint is not free from criticism. Stress concentrations occur mainly at well-defined boundaries, which do not naturally appear in homogenization-based approaches with intermediate densities. Thus, local high stress concentrations may remain "invisible" in some cases. In spite of this, the example in Sect. 8.2 shows that the formulation is sensitive to local high stresses and is capable of avoiding them. Moreover, the last criticism also applies to the compliance-based approach, whose designs need to satisfy some failure criterion for practical purposes. Within this context, the present approach seems to define more adequate designs than the former formulations when material failure criteria are imposed.

Acknowledgements The authors are grateful to Ana Friedlander Martínez, Sandra A. Santos and José M. Martínez (IMECC/UNICAMP) for helpful discussions about the opti-

mization algorithm and its QUACAN implementation. We also thank the TACSOM (Theoretical, Applied and Computational Solid Mechanics Group) group (www.lncc.br/~ tacsom) for the computational facilities of the ACDPOOP/ACDPFEM system.

This work was partially supported by the PICDT/CAPES program and by the Federal Technology Education Center of Paraná CEFET/PR-DAMEC, and by the Project Nos. CNPq. 467669/00-0, 523564/96-1 and 523728/94-8.

References

Bendsøe, M.P. 1995: *Optimization of structural topology, shape, and material*. Berlin, Heidelberg, New York: Springer-Verlag

Bendsøe, M.P.; Kikuchi, N. 1988: Generating optimal topologies in structural design using a homogenization method. *Comput. Methods Appl. Mech. Eng.* **71**, 197–224

Bendsøe, M.P.; Sigmund, O. 1999: Material interpolation schemes in topology optimization. *Arch. Appl. Mech.* **69**, 635–654

Bertsekas, D.P. 1996: *Constrained optimization and Lagrange multiplier methods*. Belmont: Athena Scientific

Bielschowsky, R.H.; Friedlander, A.; Gomes, F.A.M.; Martínez, J.M.; Raydan, M. 1997: An adaptive algorithm for bound constrained quadratic minimization. *Investigación Operativa* **7**, 67–102

Borrvall, T. 2001: Topology optimization of elastic continua using restriction. *Arch. Comput. Methods Eng.* **190**, 4911–4928

Borrvall, T.; Petersson, J. 2001: Topology optimization using regularized intermediate density control. *Comput. Methods Appl. Mech. Eng.* **190**, 4911–4928

Bulman, S.; Sienz, J.; Hinton, E. 2001: Comparisons between algorithms for structural topology optimization using a series of benchmarks studies. *Comput. Struct.* **79**, 1203–1218

Chen, W.F.; Han, D.J. 1988: *Plasticity for structural engineers*. New York: Springer Verlag

Cheng, G.D.; Guo, X. 1997: ε–Relaxed approach in structural topology optimization. *Struct. Optim.* **13**, 258–266

Cheng, G.D.; Jiang, Z. 1992: Study on topology optimization with stress constraints. *Eng. Optim.* **20**, 129–148

Sousa de Cursi, J.E.; Pagnaco, E. 1995: Minimun mass parts in 2D elasticity. In: Rozvany, G; Olhoff, N. (eds.) *WCSMO I – Proc. 1st World Congress of Structural and Multidisciplinary Optimization* (held in Goslar, Germany), pp. 231–236. Oxford: Pergamon Press

Duysinx, P. 1998: Topology optimization with different stress limits in tension and compression. *Internal report: Robotics and Automation*, Institute of Mechanics, University of Liege, Liege, Belgium

Duysinx, P.; Bendsøe, M.P. 1998: Topology optimization of continuum structures with local stress constraints. *Int. J. Numer. Methods Eng.* **43**, 1453–1478

Duysinx, P.; Sigmund, O. 1998: New developments in handling stress constraints in optimal material distribution. In: *7th AIAA/USAF/NASA/ISSMO Symposium on Multidisciplinary Design Optimization* (held in Saint Louis, MI, USA), pp. 98/4906/1–9. Reston: American Institute of Aeronautics and Astronautics

Friedlander, A.; Martínez, J.M.; Santos, S.A. 1994: A new trust-region algorithm for bound constrained minimization. *Appl. Math. Optim.* **30**(3), 235–266

Haber, R.B.; Jog, C.S.; Bendsøe, M.P. 1995: The perimeter method – a new approach to variable topology shape design. In: Rozvany, G; Olhoff, N. (eds.) *WCSMO I – Proc. 1st World Congress of Structural and Multidisciplinary Optimization* (held in Goslar, Germany), pp. 153–160. Oxford: Pergamon Press

Haug, E.J.; Choi, K.K.; Komkov, P.V. 1986: *Design sensitivity analysis of structural systems*. Orlando: Academic Press

Kirsch, U. 1990: On singular topologies in optimal structural design. *Struct. Optim.* **2**, 133–142

Michell, A.G.M. 1904: The limits of economy of material in frame structures. *Philos. Mag.* **8**, 589–597

Novotny, A.A.; Fancello, E.A.; Souza de Cursi, J.E. 1998: An h adaptive topological optimization design in 2D elasticity. In: Idelsohn, S.; Oñate, E.; Dvorkin, E. (eds.) *WCCM IV – Proc. 4th World Congress on Computational Mechanics* (held in Buenos Aires). Barcelona: Centro Internacional de Métodos Numéricos en Ingeniería

Park, Y.K. 1995: *Extensions of optimal layout design using the homogenization method*. Ph.D. thesis, The University of Michigan, Ann Arbor, MI, USA

Payten, W.M.; Ben-Nissan, B.; Mercer, D.J. 1998: Optimal topology design using a global self-organizational approach. *Int. J. Solids Struct.* **35**(3–4), 219–237

Pereira, J.T. 2001: *Otimização Topológica de Componentes Mecânicos com Restrições sobre o Critério de Falha Material*. Ph.D. thesis, GRANTE – Grupo de Análise e Projeto Mecânico, Departamento de Engenharia Mecânica, Universidade Federal de Santa Catarina, Florianópolis, SC, Brazil

Petersson, J. 1999: Some convergence results in perimeter-controlled topology optimization. *Comput. Methods Appl. Mech. Eng.* **171**, 123–140

Petersson, J.; Sigmund, O. 1998: Slope constrained topology optimization. *Int. J. Numer. Methods Eng.* **41**, 1417–1434

Querin, O.M.; Steven, G.P.; Xie, Y.M. 2000: Evolutionary structural optimization using additive algorithm. *Finite Elem. Anal. Des.* **34**, 291–308

Querin, O.M.; Young, V.; Steven, G.P.; Xie, Y.M. 1998: Computational efficiency and validation of bidirectional evolutionary structural optimisation. In: Idelsohn, S.; Oñate, E.; Dvorkin, E. (eds.) *WCCM IV – Proc. 4th World Congress on Computational Mechanics* (held in Buenos Aires). Barcelona: Centro Internacional de Métodos Numéricos en Ingeniería

Raghava, R.; Caddell, R.M.; Yeh, G.S.Y. 1973: The macroscopic yield behaviour of polymers. *J. Mater. Sci.* **8**, 225–232

Shim, P.Y.; Manoochehri, S. 1997: Generating optimal configurations in structural design using simulated annealing. *Int. J. Numer. Methods Eng.* **40**, 1053–1069

Shim, P.Y.; Manoochehri, S. 1998: Optimal configuration design of structures using the binary enumeration technique. *Finite Elem. Anal. Des.* **31**, 15–32

Stolpe, M.; Svanberg, K. 2001: Modelling topology optimization problems as mixed 0-1 programs. *Internal Report KTH/OPT SYST/FR 01/10 SE, KTH – Optimization and Systems Theory*, Department of Mathematics, Royal Institute of Technology, Stockholm, Sweden

Sved, G.; Ginos, Z. 1968: Structural optimization under multiple loading. *Int. J. Mech. Sci.* **10**, 803–805

Yang, R.J.; Chen, C.J. 1996: Stress–based topology optimization. *Struct. Optim.* **12**, 98–105

Yang, R.J.; Chuang, C.H. 1994: Optimal topology design using linear programming. *Comput. Struct.* **52**(2), 265–275

Appendix: Gradient of the ϵ-relaxed function constraint

It is a usual approach in elastoplasticity to write the failure function of any isotropic material $F(\sigma)$ as

$$F(I_1,\ J_2,\ J_3,\ k_1,\ k_2,\ \dots) = 0\,, \tag{A.1}$$

where k_1 and k_2, are material parameters, and I_1, J_2 and J_3 are the three invariants of the stress tensor σ given by

$$I_1 = \sigma_{kk}\,, \quad J_2 = \frac{1}{2}S_{ij}S_{ij}\,, \quad J_3 = \frac{1}{3}S_{ij}S_{jk}S_{ki}\,.$$

The tensor S denotes the deviatoric stresses and is given by $S_{ij} = \sigma_{ij} - \frac{1}{3}\sigma_{kk}\delta_{ij}$, δ_{ij} being the Kronecker tensor.

The derivative of the ϵ-relaxed constraint (13) related to the symmetric displacement gradient $\nabla^S\mathbf{u}$ may be written using the chain rule as

$$\frac{\partial g_\epsilon(\rho,\sigma)}{\partial \nabla^S\mathbf{u}} = \rho\frac{\partial F\left(\sigma\left(\nabla^S\mathbf{u}\right)\right)}{\partial \nabla^S\mathbf{u}} = \rho\frac{\partial F(\sigma)}{\partial\sigma}\frac{\partial\sigma}{\partial\nabla^S\mathbf{u}}\,. \tag{A.2}$$

As shown by Chen and Han (1988), the derivative of the failure function on the stress space may be expressed in the following simplified form:

$$\begin{aligned}\frac{\partial F(\sigma)}{\partial\sigma_{ij}} &= \frac{\partial F(\sigma)}{\partial I_1}\frac{\partial I_1}{\partial\sigma_{ij}} + \frac{\partial F(\sigma)}{\partial J_2}\frac{\partial J_2}{\partial\sigma_{ij}} + \frac{\partial F(\sigma)}{\partial J_3}\frac{\partial J_3}{\partial\sigma_{ij}} \\ &= B_1\delta_{ij} + B_2S_{ij} + B_3t_{ij}\,,\end{aligned} \tag{A.3}$$

where the second-order tensor t is given by $t_{ij} = S_{ik}S_{kj} - \frac{2}{3}J_2\delta_{ij}$. Note that once the current stress state σ is given, the scalars B_1, B_2 and B_3 are easily obtained from the explicit failure function:

$$B_1 = \frac{\partial F}{\partial I_1}\,, \qquad B_2 = \frac{\partial F}{\partial J_2}\,, \qquad B_3 = \frac{\partial F}{\partial J_3}\,. \tag{A.4}$$

To complete the RHS of (A.2), it is necessary to compute

$$\frac{\partial\sigma}{\partial\nabla^S\mathbf{u}} = \frac{\partial}{\partial\nabla^S\mathbf{u}}\left(D^0\nabla^S\mathbf{u}\right) = D^0\,.$$

Combining this result with (A.3) the following expression is obtained:

$$\frac{\partial g_\epsilon(\rho,\sigma)}{\partial\nabla^S\mathbf{u}} = \rho H^\sigma\,, \tag{A.5}$$

where H^σ is a second-order symmetric tensor given by

$$H^\sigma_{ij} = 2G\left[\frac{(1+\nu)}{(1-2\nu)}B_1\delta_{ij} + B_2S_{ij} + B_3t_{ij}\right]. \tag{A.6}$$